STRUCTURE, PHASE TRANSFORMATIONS, AND DIFFUSION

Electron Microscopy Study of Metastable Shape Memory Cu−Al−Ni Alloys

V. G. Pushin[a, b], *, N. N. Kuranova[a, b], V. V. Makarov[a], A. E. Svirid[a], and A. N. Uksusnikov[a]

[a] *Mikheev Institute of Metal Physics, Ural Branch, Russian Academy of Sciences, Ekaterinburg, 620108 Russia*

[b] *Yeltsin Ural Federal University, Ekaterinburg, 620002 Russia*

*e-mail: pushin@imp.uran.ru

Abstract—Data on premartensitic states and martensitic transformations in the shape memory alloys Cu−14 wt % Al−3 wt % Ni and 13.5 wt % Al−3.5 wt % Ni were obtained using electron microscopy and X-ray analysis together with measurements of electrical resistivity and magnetic susceptibility. The fine structure and diffuse electron scattering have been studied in detail, including in situ heating and cooling experiments. On the basis of the observed diffuse scattering and internal defects of the martensitic substructure, a crystallographic model of martensitic rearrangement $\beta_1 \to \beta_1'$ and $\beta_1 \to \gamma_1'$ is suggested.

INTRODUCTION

External temperature, forces, and magnetic and electric fields induce thermoelastic martensitic transformations (TMT), which give rise to a series of extraordinary and extremely important physical phenomena in various materials. The TMT-induced cyclic reversible shape-memory effects (SME), giant superelasticity, and damping, which can be reproduced once or repeatedly, are characteristic of so-called smart alloys belonging to a new type of structural multifunctional materials [1−6]. Recently, it has been discovered that these materials also exhibit giant caloric effects, i.e., magnetocaloric, electrocaloric, barocaloric, elastocaloric, which are employed in efficient eco-friendly refrigeration technologies [7−10].

The rapid development of modern technology requires such smart alloys that can be applied in products, devices, and mechanisms in a wide range of temperature, force, and other operating conditions. At the same time, many polycrystalline smart materials (except for binary titanium nickelide alloys) have a significant drawback, i.e., low ductility and brittleness, which impedes application of their unique properties even in a single use rather than in a repeated cyclic mode. Therefore, in order to extend the scope of industrial applications, methods of primary synthesis and search for optimal alloying and thermomechanical processing of various polycrystalline smart materials for their plasticizing require urgent development.

Thus, copper β alloys (Cu−Al−Ni, Cu−Zn−Al, Cu−Zn−Sn) are less expensive SM alloys experiencing TMTs and characterized by better thermo- and electric conductivities, as well as easier processing routine compared with titanium nickelide alloys [1−4]. Moreover, they demonstrate excellent SME characteristics in a single-crystal state. However, in a coarse-grained state, these polycrystalline alloys have extremely low ductility, crack resistance, and fatigue life [2, 3, 11, 17]. This impedes the implementation of SMEs typical of their single crystals. In this case, one of the key factors preventing the application of these shape-memory (SM) alloys is their intercrystalline brittleness.

Previously, it has been shown that the strength and plasticity of SM titanium-nickelide-based alloys are considerably improved via the formation of ultrafine-grained (UFG) structure [12]. The UFG structure is formed by advanced methods of thermal deformation using different methods of severe plastic deformation (SPD), including multipass rolling, drawing into strip, rods, or wires of Ti−Ni alloys.

In [12−16], we demonstrated that, upon the SPD, the embrittlement of SM copper alloys significantly weakens due to a drastic decrease in the grain size and subsequent increase in the length of their boundaries. Various other methods, such as doping, heat treatment, rapid quenching, powder metallurgy, and many others were unsuccessful and did not noticeably refine
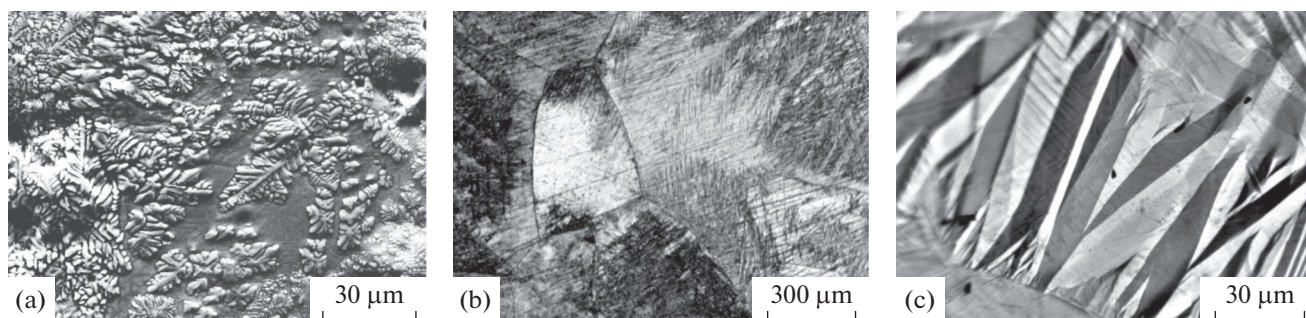
Fig. 1. SEM images of back scattered electrons (a) and OM images (b, c) of Cu−13.5Al−3.5Ni alloys (a, c) and Cu−14Al−3Ni (b) in as-cast (a), austenitic (b), and martensitic (c) states.

the grain structure of these alloys or improve their ductility [11].

Finally, the key role of premartensitic phenomena should be noted not only in realization of thermoelastic mechanism of nucleation and subsequent growth of martensitic crystals, but also in the physicomechanical behavior of metastable alloys upon the TMT under various conditions [1−6]. It is known that copper β alloys in the premartensitic state experience a strong softening of the elastic modulus C' and increase in the elastic anisotropy A [6, 17]; however, they are not fully studied by modern high-resolution structural methods of electron microscopy combined with selected-area diffraction [6, 18]. Therefore, this work aims to study structural features of the premartensitic state of metastable Cu−Al−Ni alloys upon the TMT.

MATERIALS AND METHODS

Two alloys were prepared, i.e., Cu−14% Al−3% Ni (in austenitic state at room temperature (RT)) and Cu−13.5Al−3.5Ni (in martensitic state at RT). They were melted using high-pure components Cu, Al, Ni (99.99% purity). Chemical composition of the alloys in wt % was determined by the spectral analysis. The Cu−14Al−3Ni alloy contains 13.95% Al, 3.02% Ni, balance Cu; the Cu−13.5 Al−3.5 Ni alloy contains 13.40% Al, 3.36% Ni, 0.05% Fe, balance Cu. Ingots were subjected to hot forging at 1173−1273 K into rods with a cross-section of 20 × 20 mm and to quenching from 1223 K in water (after holding for 10 min). Critical temperatures of the start (M_s, A_s) and finish (M_f, A_f) of the direct (M_s, M_f) and reverse (A_s, A_f) TMTs were determined via cyclic temperature measurements of magnetic susceptibility $\chi(T)$ and electrical resistivity $\rho(T)$ with the a heating rate of approximately 5 K/min. The structure and phase composition were studied by X-ray diffraction analysis, optical metallography (OM), transmission electron microscopy (TEM) using Tecnai G^2 30 with accelerating voltage of 300 kV, and scanning electron microscopy (SEM) using a Quanta-200 Pegasus microscope at an accelerating

voltage of 30 kV. X-ray analysis was carried out in monochromatic CuK_α irradiation.

RESULTS

As has been shown previously, as-cast and hot-forged copper β alloys under consideration upon further cooling in air decompose as follows: $\beta \rightarrow \beta_1 + \gamma_2$ (at temperatures above T_{ED}, in the vicinity of 840 K) and undergo the eutectoid decomposition $\beta_1 \rightarrow \alpha + \gamma_2$ (at temperatures below T_{ED}) (Fig. 1a), which agrees with the known data [2, 3]. However, their quenching after hot forging can prevent the eutectoid decomposition. Figure 1 shows typical OM images of the grain microstructure in β_1 austenite (Fig. 1b) and pairwise-twinned crystals of martensite of intragranular packet pyramidal morphology (Fig. 1c) in quenched Cu−13.5 Al−3.5 Ni and Cu−14 Al−3 Ni.

As is known, above T_{ED} and M_s, β austenite experiences two successive disorder-order phase transitions $(\beta \rightarrow \beta_2(B2) \rightarrow \beta_1(D0_3))$ [2, 3]. Due to the multinucleation transition, a special substructure of the so-called antiphase domains is formed, which can be recognized by their boundaries (antiphase boundary APB) in the dark-field TEM images of superstructure reflections (Fig. 2). In this case, the martensitic structure inherits the long-range atomic order of the initial ordered austenitic phase, which determines its important role in orientational structural reversibility of crystals and phase thermoelasticity upon the TMT [1−3].

The APBs, including those of the labyrinth morphology, have predominantly crystallographic faces in {100} and {110} planes of cuboid domains (Fig. 2).

Usually, inside them, in a "Swiss cheese" manner, there are more disperse oval domains in a probable form of rhombododecahedrons with faces along {111} [19]. In TEM analysis, bright- and dark-field images of austenite also show a tweed diffraction contrast (Figs. 2, 3). The tweed contrast was naturally extinguished under certain diffraction conditions, set by sample tilting in a goniometer. According to the analysis, the tweed regions are oriented along various crys-
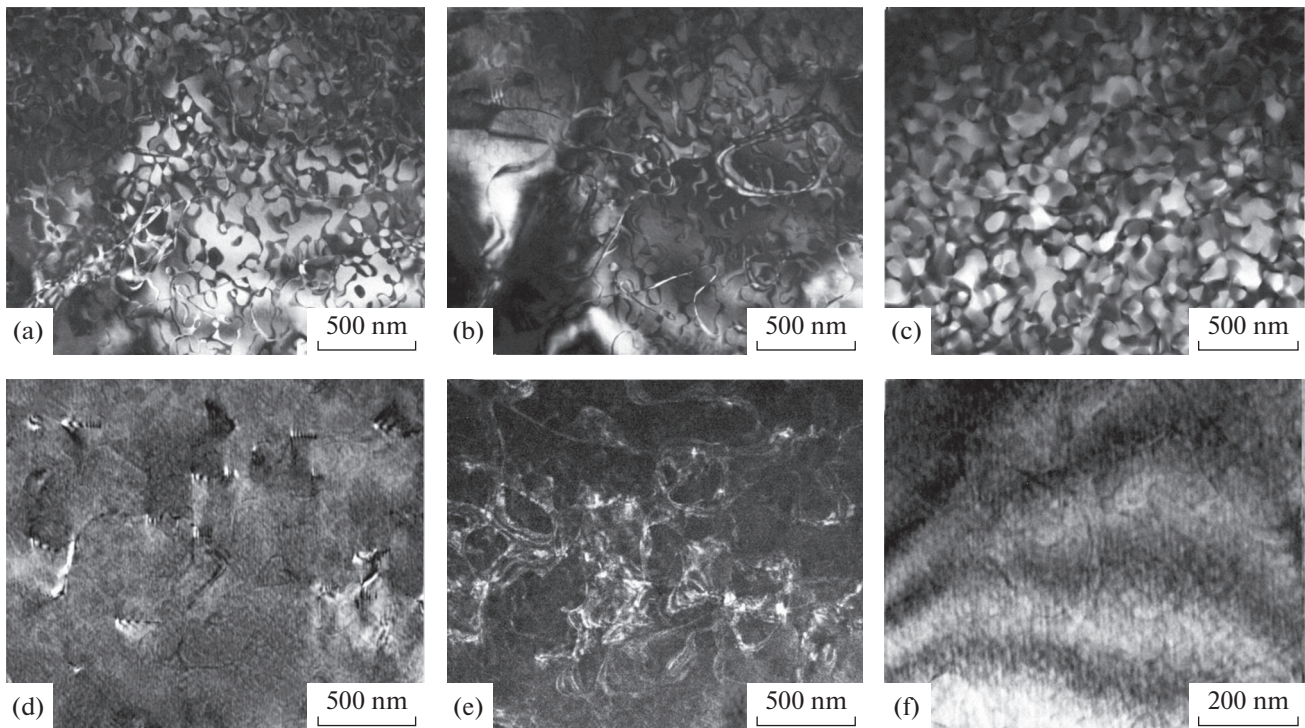
Fig. 2. Dark-field TEM images of tweed contrast of superstructure 200 (a–c) and structural 220 (d–f) reflections of Cu−14Al−3Ni alloy. Zone axis of the reflecting planes is close to [100] $D0_3$.

tallographic directions, which are mainly intersections of the {110} planes and foil surface. It has a fine structure of equiaxial and platelike elements of alternating uniform contrast, whose size depends on the diffraction conditions (Fig. 3c). It often serves as a background for dislocation and APBs contrast (see Figs. 2, 3). In this case, at the APBs, the contrast and size of tweed elements are enhanced, which indicates their heterogeneous localization along certain coherent superstructure subboundaries (Fig. 3e). Such enhancement of the tweed contrast is also found in images of dislocations that can be either inclined or positioned horizontally (Figs. 3d, 3f).

In the selected-area electron diffraction (SAED) patterns, along with Bragg reflections, a complex picture of diffuse scattering is observed, whose reconstruction in the reciprocal lattice reveals positions of the planar diffuse layers {111}* which pass through all hkl nodes, excluding the central node 000 (Figs. 4, 5) [6, 18]. The intensity distribution of diffuse scattering in these {111}* layers is nonuniform and regularly changes with their position in the reciprocal lattice. The scattering is more intensive in the vicinity of reflections than between them. The scattering does not occur (except for double diffraction), when the diffraction vector g is parallel to the diffuse layer plane (vector g belongs to the plane passing through the center of the reciprocal lattice). In the reciprocal lattice, the most intense diffuse strands avoid radial directions $\langle 110 \rangle$*. An additional evidence of the enhanced intensity of the strands along $\langle 110 \rangle$* is their diffuse spotlike shape, when in the reciprocal lattice the strands form an angle with the diffraction plane and pierce the Ewald sphere. Such piercings are caused by the existence of inclined strands along $\langle 110 \rangle$* both in the vicinity of Bragg reflections and between them (e.g., $1/2 \langle 112 \rangle$* in the following cross-sections of reciprocal lattice {110}*, {311}* or {210}*). It is typical of diffuse scattering effects to retain their sufficiently high intensity with increasing diffraction angle in comparison with attenuating Bragg reflections. Such scattering has already been observed in situ at temperatures higher than M_s by 100−150 K (Figs. 3, 4).

As M_s is approached, the intensity of strands along $\langle 110 \rangle$* increases, and, besides, what is the most important, according to the qualitative and quantitative assessments, extra reflections (or satellites) in the reciprocal lattice positions close to $1/2 \langle 110 \rangle$*, $1/3 \langle 110 \rangle$*, $1/6 \langle 110 \rangle$* are also enhanced, while on strands, $\langle 112 \rangle$* − $1/2 \langle 112 \rangle$*, $1/3 \langle 112 \rangle$* (Fig. 5). At this satellite stage of long-period modulation of the crystal lattice, several lattice waves of atomic displacements are distinguished and described by wave vectors $\pm k$ and their polarization vectors e_k. According to experimental data, there are the following modes of atomic displacements: the transverse wave with $k = 1/2 \langle 110 \rangle$*, e_k is parallel to $\langle 1\bar{1}0 \rangle$; the transverse wave with $k_1 = 1/6 \langle 110 \rangle$*, $\mathbf{e_k}$ is parallel to $\langle 1\bar{1}0 \rangle$; and the transverse wave with $k_2 = 1/3 \langle 110 \rangle$*, e_k is parallel to $\langle 1\bar{1}0 \rangle$.
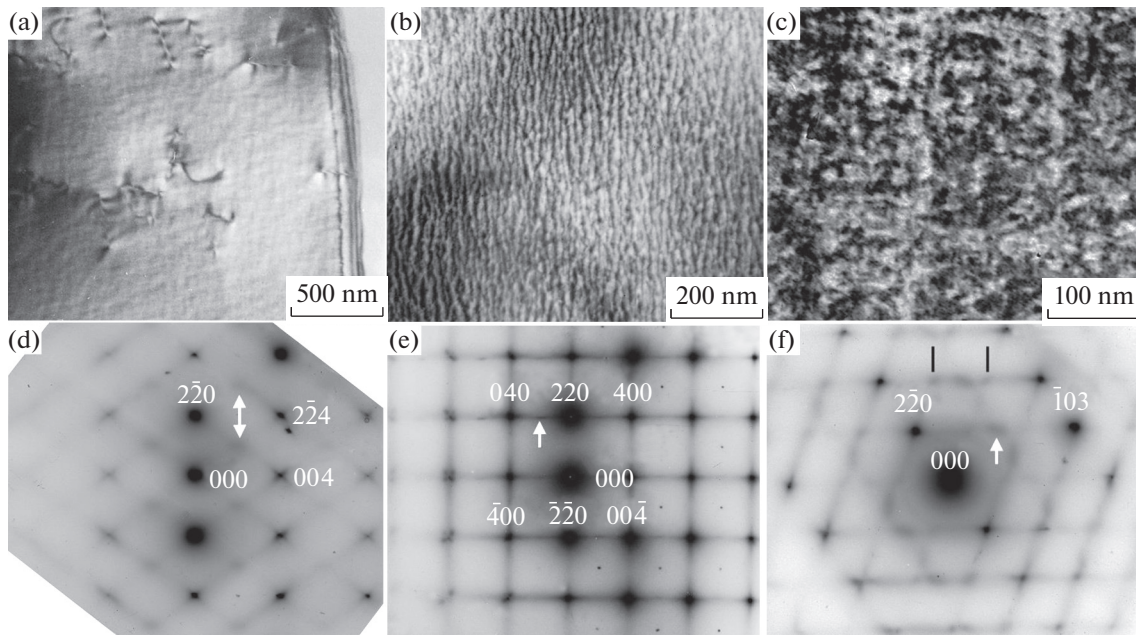
Fig. 3. Dark-field TEM images of structure reflections 220 of the deformation tweed contrast (a–c) in β_1 austenite of Cu−14Al−3Ni alloy and corresponding SAEDs, zone axis (e) [001], (d) [110], (f) [331] $D0_3$. Experiments are carried out at 450 K (a, d) and at room temperature (RT) (b, c, e, f).
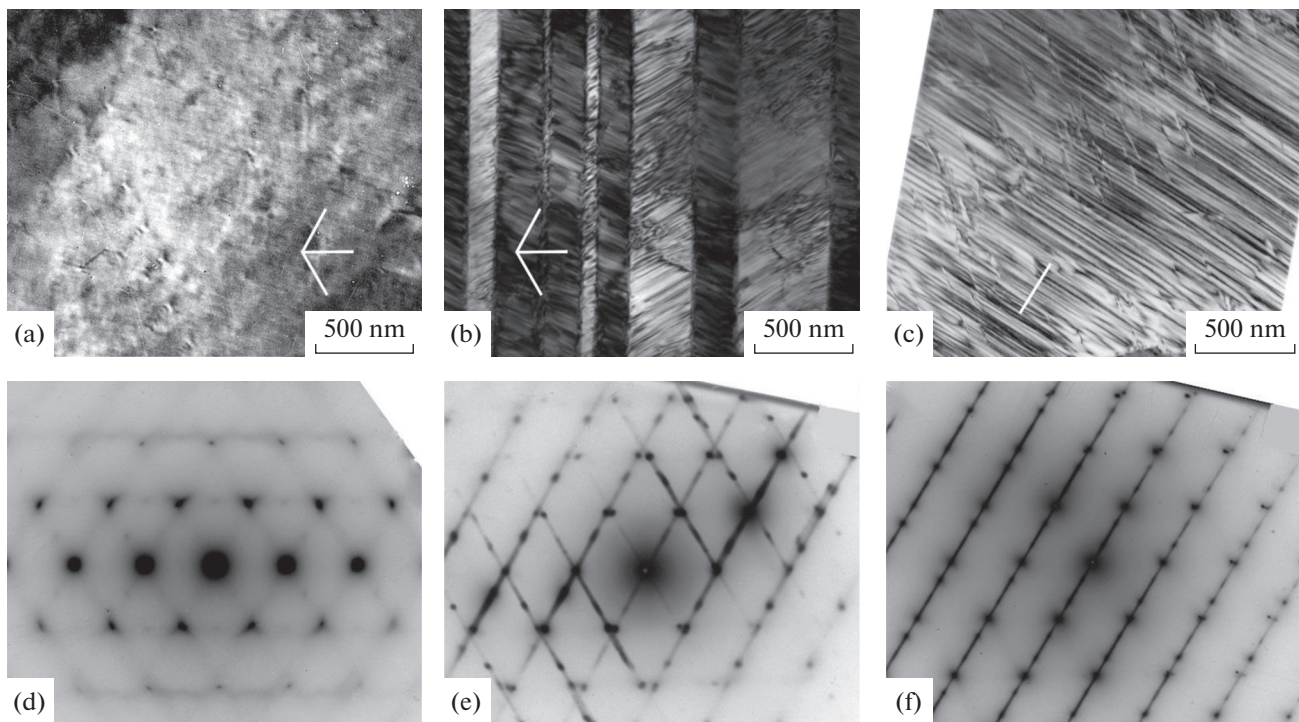

Fig. 4. Dark (a) and bright (b, c) field TEM images of the deformation tweed contrast of β_1 austenite (a); SF of martensite γ_1' (b) and β_1' (c) of Cu−13.5Al−3.5Ni alloy, as well as corresponding SAEDs (d–f), zone axis close to [111] $D0_3$. Experiments are carried out at 450 K (a, d) and at the RT (b, c, e, f).
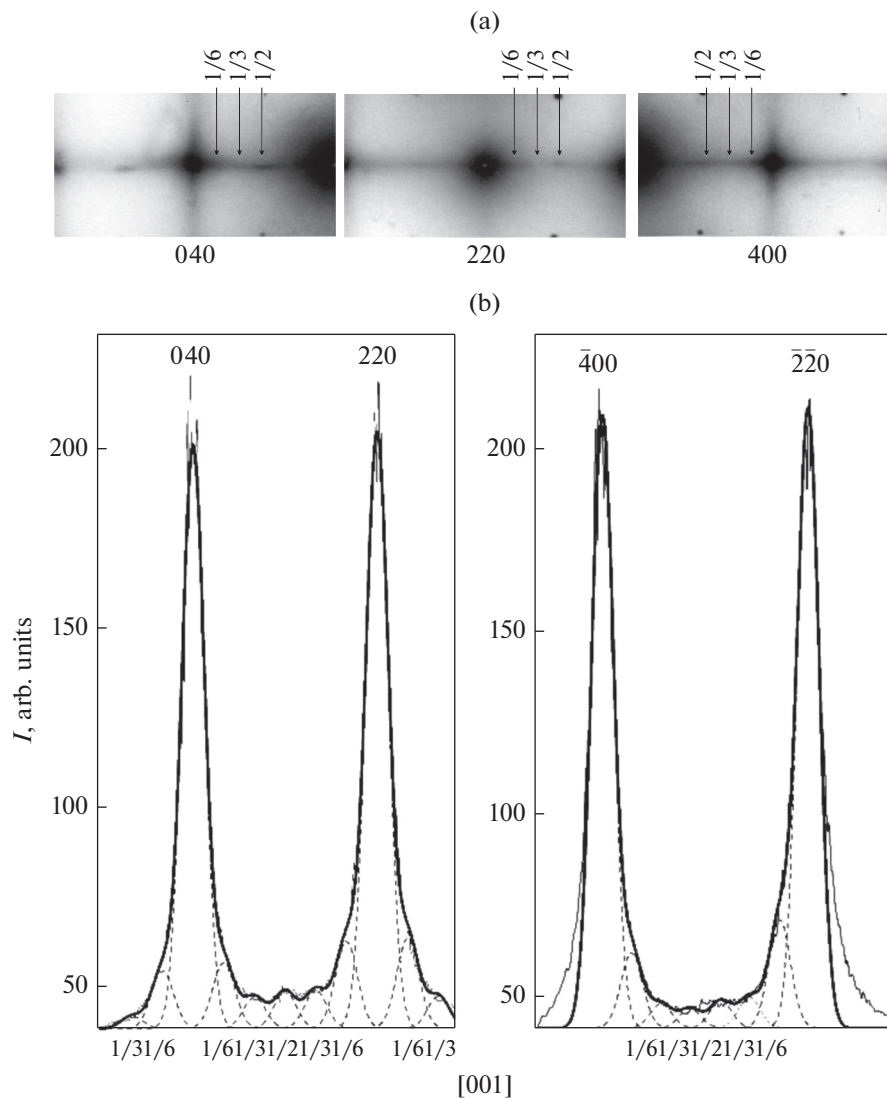
(a)

040　　　　　　　220　　　　　　　400

(b)

[001]

Fig. 5. Fragments of the SAED with zone axis [001] with diffuse effects (a) and intensity profiles upon scanning of the diffuse scattering along strands with the satellites: 1/6 ⟨220⟩, 1/3 ⟨220⟩, 1/2 ⟨220⟩ (b). Solid thin lines represent experimental profiles which were obtained with the Digital Micrograph software upon SAED indexing. Solid bold lines represent intensity profiles which were calculated for main reflections using Gauss function in the Origin software. Dashed lines represent calculated profiles for satellites: 1/6 ⟨220⟩, 1/3 ⟨220⟩, 1/2 ⟨220⟩. Bragg reflections 400 and 220 are indicated.

We believe that the transverse wave with $k = 1/3\langle 112\rangle^*$ should not be considered as independent, because it is a superposition of two waves with k equal to $\langle 1/3\ 1/3\ 0\rangle^*$ and $\langle 1/3\ 0\ 1/3\rangle^*$ (forming satellites in the diffraction pattern $1/3\langle 211\rangle^*$). Previously, we have already discussed the ambiguous circumstances of the nature of diffuse effects of the $1/2\langle 112\rangle^*$ type.

Thus, the typical features of the observed deformation tweed contrast and diffuse scattering of electrons, i.e., its periodicity, regular extinctions and amplifications, allows their identification as localized transverse and longitudinal short- and long-wave atomic displacements, which periodically distort the initial crystal lattice. The spectra of atomic displacement waves in the k-space of the reciprocal lattice are shown in Fig. 6. Interpretation of the obtained data allows us to construct a physical model of the real microstructure with its evolution, as well as to establish its crucial effect on the TMT of the Cu–Al–Ni alloys.

In alloys with a bcc lattice, the scattering between reflections in the form of planar diffuse $\{111\}^*$ layers is caused by short-wavelength acoustic uncorrelated displacements of atomic chains closely packed along $\langle 111\rangle$ relative to each other, which prevail in the vibration spectrum. With the premartensitic softening of the elastic moduli, especially C' [6, 17], the amplitudes and correlations of such peculiar linear defects of atomic displacements gradually increase, primarily in the closely packed $\{110\}$ planes.
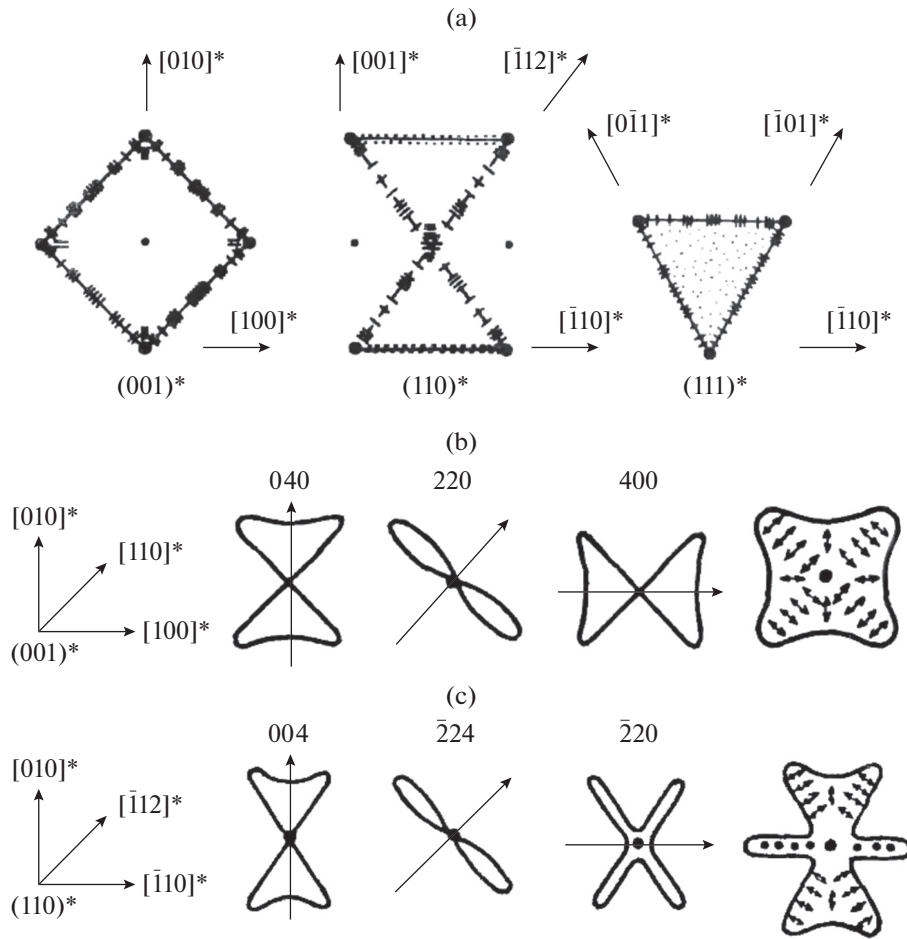
(a)

(b)

(c)

Fig. 6. Atomic displacement wave spectra in the form of plane cross-sections (001)*, (110)*, and (111)* of reciprocal k-space (a) and in the vicinity of reciprocal lattice nodes of the planes (001)* and (110)* (b, c). Projections of e_k for k wave of enhanced amplitude and, consequently, more intensive diffuse scattering are marked by dots, arrows, and dashes.

If the correlations of atomic displacements in these planes are stronger than those of planes relative to each other, the diffuse scattering has the form of continuous strands along $\langle 110 \rangle^*$. Taking into account the nature of the tweed contrast, the atomic displacements prefer to localize themselves in nanodomains, and their distorted structure and symmetry can be described by the short-range order of atomic displacements (SROAD) [6, 12]. In this case, the long-wave (homogeneous in the limit) atomic displacements can be determined from the analysis of small-angle diffuse scattering in the vicinity of Bragg reflections and their extinctions (see Figs. 6b, 6c). Similar to short-wave displacements, they can be described by the wave spectrum of vectors k and e_k in the vicinity of reciprocal lattice nodes. Here, the presence of longitudinal displacement $\langle 100 \rangle^*$, $\langle 100 \rangle^*$ waves, which are responsible for the longitudinal Bane distortion, attracts attention.

When, upon cooling of the alloys, below a certain temperature T_{IS}, satellites appear in the diffraction pattern, and a new stage of the interphase transformation of the austenitic structure begins, which we designate as the stage of weakly incommensurate satellites. These are mainly satellites of the "1/6," "1/3," and "1/2" types, corresponding to the long-period modulated shear nanostructures, intermediate shear substructures ISS-I (for satellites of the "1/6" and "1/3" types) and ISS-II (for "1/2" type satellites) (Figs. 3–5) [12]. The satellite stage is distinguished as an independent state that succeed the SROAD and is characterized by the pairwise ordered intermediate shear substructures (ISS) (Fig. 7). At the same time, since all crystallographically equivalent variants of distortion nanodomains (orientational and antiphase) are statistically distributed over the austenitic phase, on the average, the structure of such metastable alloys retains the initial cubic symmetry.

According to the diffraction data, the internal distortion and local symmetry of the ISS-domains differ from the initial symmetry of austenite and, obviously, approach the structure of developing martensitic
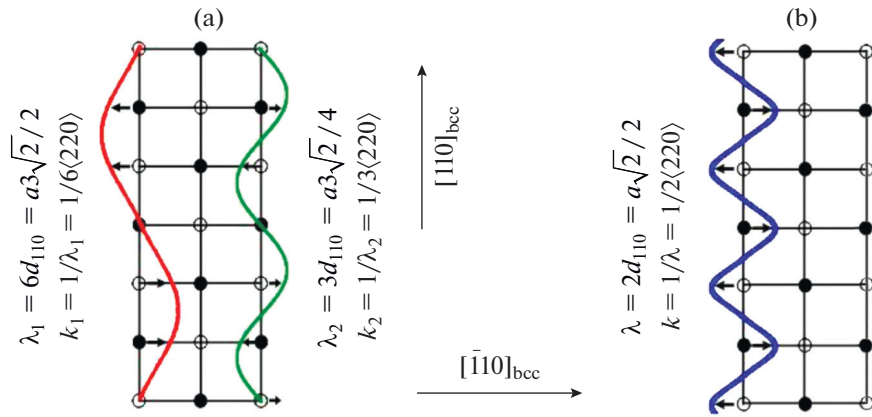
Fig. 7. Shuffle schemes promoting $D0_3$ cubic lattice transformations via ISS-I (a) and ISS-II (b).

phases to the maximum extent while maintaining coherent coupling under specific conditions of progrssively growing instability and anharmonicity of the austenite local lattice [6, 12]. First, this structural mechanism of the TMT is experimentally confirmed by the fact that, in SAEDs, reflections corresponding to the developing martensitic crystals of the β_1' and γ_1' phases are located at the positions of satellites of the 1/3 and 1/2 type (see Fig. 4). Second, upon their nucleation and growth, a large number of planar chaotic stacking faults (SFs) which are parallel to the (001) basal plane appear in both β_1' and γ_1' martensitic phases. The SFs are caused by the multi-nuclei type of crystal formation from nanodomains ISS-I and ISS-II (see schemes in Figs. 7, 8). In this case, characteristic contrast (Figs. 4b, 4c) and diffuse scattering effects are observed in the form of clear solid lines passing through the martensitic Bragg reflections (Figs. 4e, 4f).

From the viewpoint of the crystal structure, the ISS domains are special "nonclassical" nanonuclei (with a structure different from structures of both austenitic and developing martensitic phases) and can act as real physical centers of nucleation of martensitic crystals. Then, at a certain synchronization of the homogeneous Bane distortion and transverse waves of static atomic displacements, which describe the structure of the ISS-I nanodomains by the 1/6 and $1/3\langle110\rangle_k\langle1\bar{1}0\rangle_e$ waves (including their possible superposition

Table 1. Critical temperatures M_s, M_f, A_s, A_f of Cu−14Al−3Ni alloys

Measurements	M_s, K	M_f, K	A_s, K	A_f, K
$\rho(T)$	250	235	265	280
$\chi(T)$	250	240	265	280

(Fig. 7a)), in the alloys under consideration, the transformation into the real martensitic β_1' (18R) structure can be observed (see Fig. 8a). When the corresponding homogeneous Bane distortion is combined with the mode of periodic shuffling of displacements of the doubling type $1/2\langle110\rangle_k\langle1\bar{1}0\rangle_e$, which form the structure of the ISS-II nanodomains (Fig. 7b), a crystal structure tends to rearrange $\beta_1 \to \gamma_1'$ (2H) (Fig. 8b). Obviously, in this case, local faults in the ideal stacking along the basal plane cause various SFs.

In conclusion, we note that in the course of thermal cycling to determine $\rho(T)$ and $\chi(T)$, i.e., cooling from RT to 90 K and heating to RT, not only the TMT hysteresis loops were determined (Table 1), but also premartensitic deviations of dependences from linear behavior were observed in the vicinity of both forward and reverse TMTs in the temperature range of 10−20 K (Fig. 9).

In addition, as has been mentioned, the copper alloys under consideration are metastable with respect to the TMT and are distinguished by the low modulus C', as well as high anisotropy of elastic moduli $A = C_{44}/C'$ (12−13 units) [17]. At the same time, e.g., elastically isotropic ductile titanium nickelide alloys with low modulus have A not greater than 1−2 units [6, 12]. The anomalously large elastic anisotropy results in prevailing localized $\langle110\rangle^*$, $\langle1\bar{1}0\rangle^*$ SROAD and ISS nanodomains in the premartensitic state, and, correspondingly, the specific morphology of nanodomains observed as regions of tweed contrast, as well as the crystallography of the shear transformation upon the TMT proceeding only via shuffling the atomic displacements $\{110\}\langle1\bar{1}0\rangle$. At the same time, variations of the long-period shear modulation of the "tripling" and "doubling" are also possible, which corresponds to two martensitic phases β_1' (18R) and γ_1' (2H).
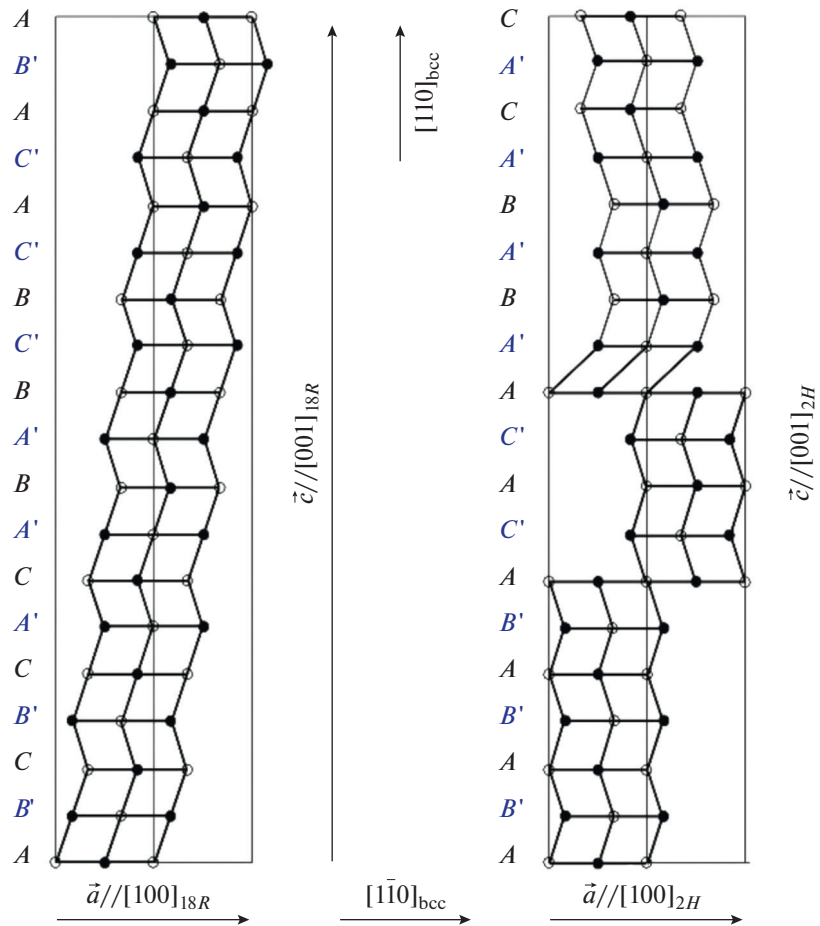
Fig. 8. Schemes of crystal lattice rearrangement of martensite: $D0_3 \rightarrow 18R$ (a) and $D0_3 \rightarrow 2H$ (b).
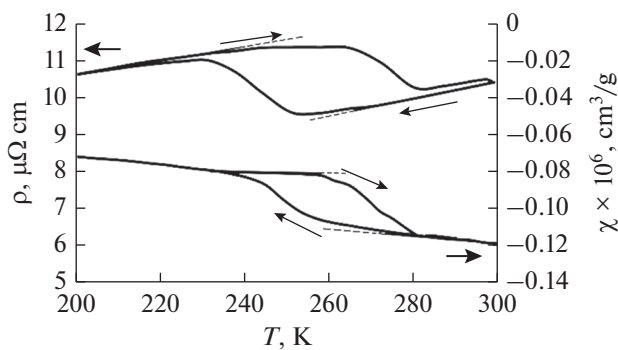

Fig. 9. Temperature dependences $\rho(T)$ and $\chi(T)$ of Cu–14Al–3Ni alloy after quenching from 1223 K into water upon thermal cycling: cooling from RT to 90 K—heating to RT.

long-period ISS-I and ISS-II structures and act as structural precursors of martensitic phases.

(2) In these alloys, a crystallographic mechanism of the nucleation and growth of martensite $\beta_1 \rightarrow \beta_1'$ and $\beta_1 \rightarrow \gamma_1'$ is proposed on the basis of the analysis of diffuse scattering and tweed contrast which arise in the premartensitic state, as well as internal defects of the martensitic substructure.

CONCLUSIONS

(1) In this work, for the first time, the effects of diffuse scattering of electrons are studied in detail using in situ transmission electron microscopy; and diffuse extra reflections (satellites) of the 1/2, 1/3, 1/6 ⟨110⟩* types are found, which originate from the intermediate

REFERENCES

1. *Shape Memory Effects in Alloys*, Ed. by J. Perkins (Plenum, London, 1975).

2. Kh. Varlimont and L. Dilei, *Martensitic Transformation in Alloys Based on Copper, Silver, and Gold* (Nauka, Moscow, 1980) [in Russian].

3. K. Ootsuka, K. Simidzu, Yu. Sudzuki, Yu. Sekiguti, Ts. Tabaki, T. Khomma, and S. Miyadzaki, *Shape Memory Alloys* (Metallurgiya, Moscow, 1990) [in Russian].

4. *Engineering Aspects of Shape Memory Alloys*, Ed. by T. W. Duering, K. L. Melton, D. Stockel, and C. M. Wayman (Butterworth-Heineman, London, 1990).

5. V. N. Khachin, V. G. Pushin, and V. V. Kondrat'ev, *Titanium Nickelide: Structure and Properties* (Nauka, Moscow, 1992) [in Russian].

6. V. G. Pushin, V. V. Kondrat'ev, and V. N. Khachin, *Pretransitional Phenomena and Martensitic Transformations* (UrBr RAS, Yekaterinburg, 1998) [in Russian].

7. E. Bonnot, R. Romero, L. Mañosa, E. Vives, and A. Planes, "Elastocaloric effect associated with the martensitic transition in shape-memory alloys," Phys. Rev. Lett. **100**, 125901 (2008).

8. A. Planes, L. Mañosa, and M. Acet, "Magnetocaloric effect and its relation to shapememory properties in ferromagnetic Heusler alloys," J. Phys.: Condens. Matter **21**, 233201 (2009).

9. J. Cui, Y. Wu, J. Muehlbauer, Y. Hwang, R. Radermacher, S. Fackler, M. Wuttig, and I. Takeuchi, "Demonstration of high efficiency elastocaloric cooling with large δT using NiTi wires," Appl. Phys. Lett. **101**, 073904 (2012).

10. L. Mañosa, S. Jarque-Farnos, E. Vives, and A. Planes, "Large temperature span and giant refrigerant capacity in elastocaloric Cu−Zn−Al shape memory alloys," Appl. Phys. Lett. **103**, 211904 (2013).

11. R. Dasgupta, "A look into Cu-based shape memory alloys: Present Scenario and future prospects," J. Mater. Res. **29**, No. 16, 1681−1698 (2014).

12. V. Pushin, N. Kuranova, E. Marchenkova, and A. Pushin, "Design and development of Ti−Ni, Ni−Mn−Ga and Cu−Al−Ni-based alloys with high and low temperature shape memory effects," Materials **12**, 2616−2640 (2019).

13. A. V. Luk'yanov, V. G. Pushin, N. N. Kuranova, A. E. Svirid, A. N. Uksusnikov, Yu. M. Ustyugov, and D. V. Gunderov, "Effect of the thermomechanical treatment on structural and phase transformations in Cu−14Al−3Ni shape memory alloy subjected to high-pressure torsion," Phys. Met. Metallogr. **119**, 374−382 (2018).

14. A. E. Svirid, A. V. Luk'yanov, V. G. Pushin, E. S. Belosludtseva, N. N. Kuranova, and A. V. Pushin, "Effect of the temperature of isothermal upsetting on the structure and the properties of the shape memory Cu−14 wt % Al−4 wt % Ni alloy," Phys. Met. Metallogr. **120**, 1159−1165 (2019).

15. A. E. Svirid, V. G. Pushin, N. N. Kuranova, E. S. Belosludtseva, A. V. Pushin, and A. V. Lukyanov, "The Effect of Plastification of Cu−14Al−4Ni Alloy with the Shape Memory Effect in High-Temperature Isothermal Precipitation," Tech. Phys. Lett. **46** (2), 118−121 (2020).

16. A. E. Svirid, A. V. Lukyanov, V. G. Pushin, N. N. Kuranova, V. V. Makarov, A. V. Pushin, and A. N. Uksusnikov, "Application of Isothermal Upset for Megaplastic Deformation of Cu−Al−Ni β Alloys," Tech. Phys. **65** (7), 1044−1050 (2020).

17. P. Sedlak, H. Seiner, M. Landa, V. Novák, P. Šittner, and L. I. Manosa, "Elastic constants of bcc austenite and 2H orthorhombic martensite in CuAlNi shape memory alloy," Acta Mater. **53**, 3643−3661 (2005).

18. K. Otsuka, C. M. Wayman, and H. Kubo, "Diffuse Electron Scattering in β−phase alloys," Metall. Trans. A **9**, 1075−1085 (1978).

19. A. M. Glezer and B. V. Molotilov, *Ordering and Deformation of Iron Alloys* (Metallurgiya, Moscow, 1984).

Translated by O. Golovnya